nature portfolio

https://doi.org/10.1038/s41586-025-09520-y

Supplementary information

ABCA7 variants impact phosphatidylcholine and mitochondria in neurons

In the format provided by the authors and unedited

Supplementary Information

Contents

Supplementary Notes

Supplementary Note 1. Description of variables according to the Rush Alzheimer's Disease Center Codebook.

1. **study**: Indicates the cohort participants were recruited through: Religious Orders Study (ROS) or Memory and Aging Project (MAP)[71].
2. **pmi**: Postmortem interval, defined as the number of hours from the participant's time of death until autopsy and tissue preservation.
3. **age_death**: Participant's age at the time of death.
4. **msex**: Participant's self-reported sex, coded as "1" for male and "0" for female.
5. **amyloid**: Mean amyloid-beta load, quantified as the percent cortical area occupied by amyloid-beta deposits via immunohistochemistry, averaged across 8 brain regions (at least 4 required): hippocampus, entorhinal cortex, midfrontal cortex, inferior temporal gyrus, angular gyrus, calcarine cortex, anterior cingulate cortex, and superior frontal cortex.
6. **ceradsc**: CERAD neuropathological score providing a semiquantitative measure of neuritic plaque density, categorized into definite AD (1), probable AD (2), possible AD (3), or no AD (4), determined independently of age or clinical data.
7. **nft**: Summary measure of neurofibrillary tangle burden, derived by microscopic assessment of silver-stained slides from five brain regions (midfrontal cortex, midtemporal cortex, inferior parietal cortex, entorhinal cortex, hippocampus), standardized regionally, and averaged into a single value.
8. **braaksc**: Semi-quantitative Braak stage score for severity and distribution of neurofibrillary tangles (NFTs), assessed with Bielschowsky silver stain in the frontal, temporal, parietal, entorhinal cortex, and hippocampus: stages I-II indicate tangles primarily in entorhinal regions; stages III-IV signify limbic involvement such as hippocampus; and stages V-VI show moderate to severe neocortical involvement.
9. **cogdx**: Final clinical consensus diagnosis regarding cognitive status at the time of death, derived by expert neurologists reviewing all available clinical data without knowledge of postmortem findings. Categories include: no cognitive impairment (1), mild cognitive impairment without other causes (2), mild cognitive impairment with another cause (3), Alzheimer's disease without another cause (probable AD) (4), Alzheimer's disease with another cause (possible AD) (5), and other primary dementia (6).
10. **niareagansc**: The NIA-Reagan neuropathological scoring system classifies Alzheimer's disease likelihood into four levels (1: high, 2: intermediate, 3: low, 4: no AD) based on combined assessment of neurofibrillary tangles (Braak) and neuritic plaques (CERAD), evaluated postmortem without knowledge of clinical dementia status.
11. **ad_reagan**: Dichotomized version of the NIA-Reagan neuropathological score, categorizing participants into Alzheimer's-positive (1: high/intermediate) or Alzheimer's-negative (0: low/no AD).

12. **apoe_genotype**: APOE genotype identified by DNA extraction from peripheral blood mononuclear cells or brain tissue, using high-throughput sequencing to genotype codon 112 and codon 158 in exon 4 of the APOE gene on chromosome 19.

Supplementary Note 2. Choosing a partitioning heuristic for gene-pathway grouping.

Methods.
The heatmap in Supplementary Figure 3a highlights how frequently pathways within a pathway database, such as WikiPathways, share gene members. On average, every pathway shown in Supplementary Figure 3a shares at least one gene with approximately 40% of the other pathways, highlighting that there is redundancy in this matrix that could be summarized in simpler terms.

To summarize redundant gene-pathway information into a limited number of non-redundant gene-pathway groups, we reformulated the gene-pathway association problem as a bipartite graph G constructed from all the genes in the Leading Edge subset (LE) and their associated pathways. LE was defined as the set of 268 genes driving the enrichment signal for pathways that passed a significance threshold of $p < 0.05$ (fGSEA) in Con vs. ABCA7 LoF excitatory neurons. G was constructed from an $n \times m$ unweighted adjacency matrix, where n represented the number of LE genes and m the number of pathways associated with four or more LE genes, as specified in the WikiPathways database[1].

Graph partitioning involves segmenting the vertices of a graph into equal-sized partitions, optimizing for the minimal number of interconnecting edges (i.e., "total cut size"). We tested three prominent graph partitioning techniques, as outlined by Elsner (1997)[72], to approximate optimal partitioning. These methods include:

1. **Recursive Spectral Bisection**: Implemented in Python using the numpy linear algebra package, this method was executed for $\log_2(N)$ iterations, yielding $N = 8$ partitions. A detailed description of the algorithm can be found in Elsner (1997)[72].
2. **Multilevel Graph Partitioning**: Leveraging the METIS software package[73] in Python using the following parameters: 'nparts=8', 'tpwgts=None', 'ubvec=None', 'recursive=False'.
3. **Kernighan-Lin (K/L) Algorithm**: Based on its original paper[74], this algorithm was implemented in Python and run with parameters set as $C = 0$, 'KL_modified=True', 'random_labels=True', 'unweighted=True', and $K = 50$.

Additionally, the Spectral Clustering algorithm, a commonly used clustering method, was applied using the 'SpectralClustering()' function from the 'sklearn' Python package with default parameters, apart from 'n_clusters=8' and 'assign_labels='kmeans''. We stipulated eight clusters for each algorithm, as qualitatively, this resolution seemed to strike a good balance to summarize main biological effects.

For benchmarking purposes, the three graph partitioning techniques and the spectral clustering algorithm were evaluated by segmenting graph G into eight gene-pathway clusters using the respective algorithms. Spectral clustering was run over 1,000 initiations, while K/L and METIS

[1]This same procedure was applied to WT vs p.Tyr622*, WT vs p.Glu50fs*3, and p.Tyr622*+/- CDP-choline comparisons, followed by K/L clustering as shown in the main figures

were run over 50,000 iterations because their solutions were slightly more variable across runs. The deterministic bisection method was run only once. A randomized graph partitioning benchmark was also computed by permuting the eight cluster labels of approximately equivalent size for 1,000 initiations. Average losses were computed per algorithm on all initiations. The benchmarking process and source code are available at our Github repository, as specified in the Code Availability section.

Results.
Spectral clustering performed significantly better than all other algorithms based on the loss (Supplementary Figure 3b). This was expected, as spectral clustering does not place a constraint on cluster size. Spectral clustering results were characterized by a single large cluster and many small clusters (Supplementary Figure 3c), indicating that this clustering algorithm was highly susceptible to outliers and suggesting that graph partitioning, which imposes the constraint of equal partitioning, was a better approach to the problem of grouping genes and pathways into biologically informative groups. Indeed, all three graph partitioning algorithms divided the graph into more uniformly-sized groups (Supplementary Figure 3c). Among the partitioning algorithms, K/L and METIS produced the most uniformly sized groups (Supplementary Figure 3c) and also had significantly lower losses compared to the spectral bisection algorithm (Supplementary Figure 3b). K/L and METIS solutions were very similar, with their respective best solutions (lowest loss) having an average Jaccard similarity index of 0.91 on the diagonal (Supplementary Figure 3d,e). K/L and METIS solutions were also consistent across pairwise random initiations, both when comparing within K/L or METIS solutions (Rand Index=0.87 and 0.91, respectively) and when comparing all pairwise K/L and METIS solutions (Rand Index=0.88) (Supplementary Figure 3f).

Overall, these experiments illustrate the utility of non-redundant gene-pathway groupings to interpret biological effects and indicate that for some gene-pathway graphs, such as the one in this study, graph partitioning is a better approach than clustering.

Supplementary Note 3. Molecular Dynamics Simulations Results.

RMSD analysis of Ala1527 vs Gly1527 in open and closed states.
To evaluate conformational stability, we conducted root mean square deviation (RMSD) analyses on ABCA7 under different states and mutations (Fig. 2f,g, Extended Data Fig. 6c,d). RMSD values for the C_α atoms were calculated over the course of a 300 ns simulation period, comparing closed and open conformations, each harboring either the G1527 or A1527 mutation.

For the open ABCA7 conformation, both the G1527 and A1527 mutants exhibited relatively minor RMSD fluctuations (Extended Data Fig. 6c,d), with RMSD values for the A1527 mutant significantly lower compared to those of the G1527 mutant (Extended Data Fig. 6e). Overall however, both mutants showed narrow RMSD distributions in the open state (Extended Data Fig. 6c,d), indicating generally stable conformational behavior.

Differences in RMSD distributions between the two variants became more pronounced in the closed state: The RMSD profile of the closed conformation with the G1527 mutation exhibited substantial fluctuations throughout the simulation (Fig. 2f), suggesting that the G1527 mutation significantly increases local structural flexibility. In contrast, the closed conformation harboring the A1527 mutation showed only minor RMSD fluctuations (Fig. 2f), suggesting that the A1527 mutation

confers greater structural stability and reduced flexibility in the closed ABCA7 conformation. Principal component analysis (PCA) further highlighted these differences visually; For the closed conformation, PCA projections of G1527 conformations over time were broad, indicating significant exploration of the conformational space (Fig. 2g). Conversely, the PCA plot for the closed A1527 mutant displayed a tightly clustered distribution (Fig. 2g), indicating limited conformational sampling over time and suggesting decreased conformational flexibility induced by the A1527 mutation.

Dihedral angle analysis of Ala1527 vs Gly1527 in open and closed states.
To further explore the local structural variations induced by a p.Ala1527Gly mutation, we analyzed backbone dihedral angles (phi/psi; ϕ/ψ) for residues 1517-1537. In the open conformation, Gly1527 consistently occupied the α-helical region of the Ramachandran plot throughout the simulation (Extended Data Fig. 7a). In contrast, Ala1527 showed two distinct populations within the α-helical region (Extended Data Fig. 7a), suggesting subtle local conformational differences, yet overall preservation of the α-helical structure. These findings align closely with the RMSD analysis, and suggest similar conformational behaviors between the variants in the open state.

However, significant structural differences emerged in the closed conformation: Ala1527 displayed two preferred conformations—one within the α-helical region and another shifted toward the β-structure region—while Gly1527 explored a broader range of dihedral angles, indicative of greater structural flexibility (Extended Data Fig. 7a,b). This observation is in line with the RMSD analysis, indicating greater structural differences specifically in the closed state, with Gly1527 exhibiting significantly greater conformational flexibility compared to Ala1527.

Secondary structure analysis of Ala1527 vs Gly1527 in open and closed states.
To complement backbone angle analysis, we also evaluated secondary structure stability throughout the simulation. In the open state, secondary structure content was comparable between variants, maintaining similar α-helical character (Extended Data Fig. 7c,d). Upon transitioning to the closed state, both variants experienced a substantial loss of α-helical content across residues 1517-1537. This loss, however, was more pronounced in the Gly1527 variant compared to the Ala1527 variant, as residues 1520-1525 retained partial α-helical structure more robustly in the Ala1527 variant compared to Gly1527 (Extended Data Fig. 7c,d).

Finally, structural alignment of the closed-state Gly1527 ABCA7 structure (PDB 8EOP) with the closed-state structures of ABCA1 (PDB 7TBW) and ABCA4 (PDB 7LKZ) revealed that residues corresponding to Gly1527 in ABCA7 (V1646 in ABCA1; I1671 in ABCA4) adopt stable α-helical structures (Extended Data Fig. 7e,f). In contrast, the Gly1527 residue in ABCA7 exhibits significant flexibility and lacks defined α-helical structure. Interestingly, our simulations indicate that the Ala1527 variant partially restores this local α-helical conformation in ABCA7 (Extended Data Figure 7c,d). These data suggest that the Gly1527 variant induces local structural changes that differentiate ABCA7 from its close homologs ABCA1 and ABCA4.

Supplementary Figures

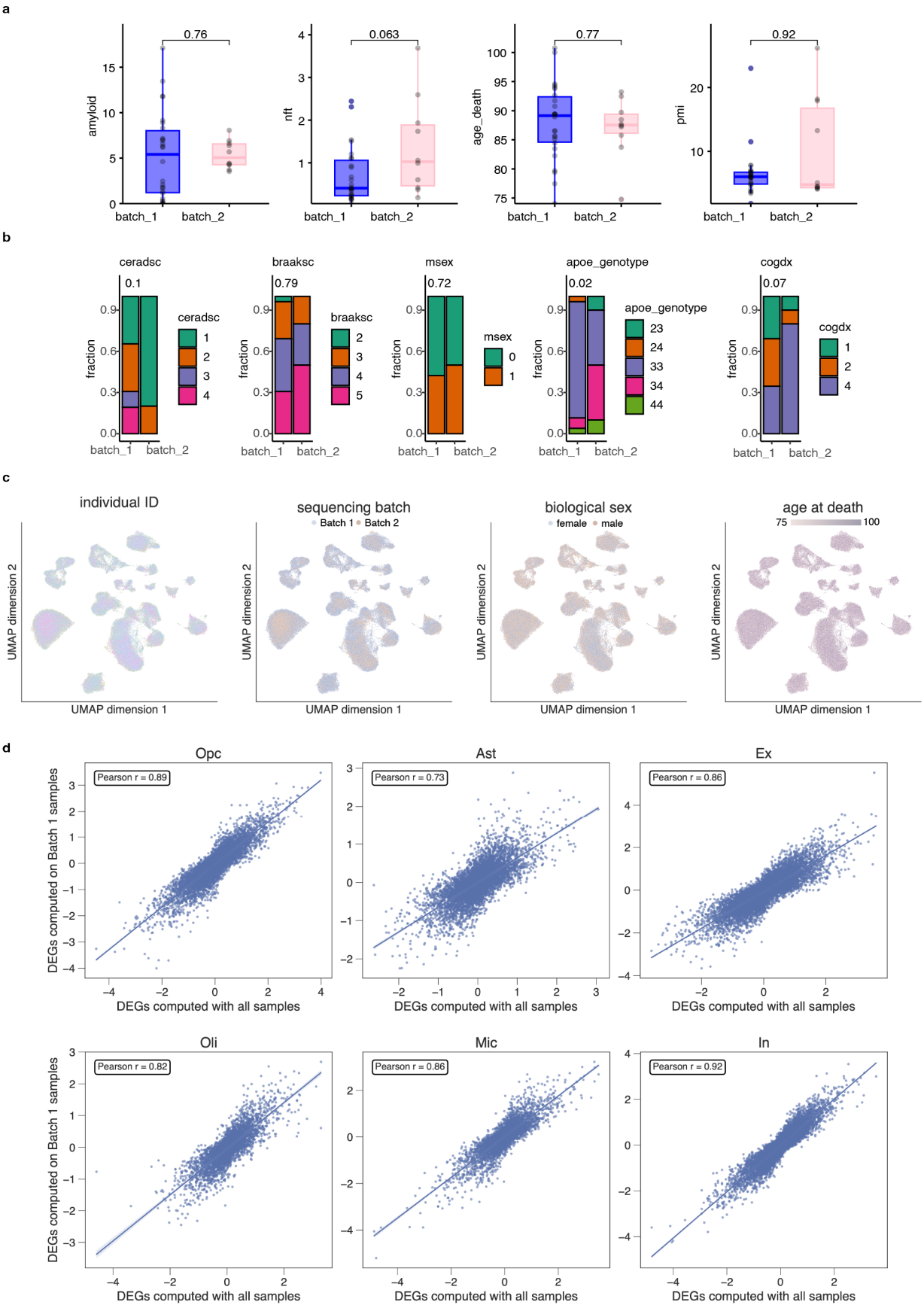
a
amyloid
0.76
nft
0.063
age_death
0.77
pmi
0.92
batch_1
batch_2
b
ceradsc
0.1
braaksc
0.79
msex
0.72
apoe_genotype
0.02
cogdx
0.07
fraction
c
individual ID
sequencing batch
Batch 1
Batch 2
biological sex
female
male
age at death
75
100
UMAP dimension 1
UMAP dimension 2
d
Opc
Ast
Ex
Oli
Mic
In
Pearson r = 0.89
Pearson r = 0.73
Pearson r = 0.86
Pearson r = 0.82
Pearson r = 0.86
Pearson r = 0.92
DEGs computed on Batch 1 samples
DEGs computed with all samples

Fig. S1. Overview of snRNA-sequencing batch correction and data quality. **a, b,** Distribution of continuous clinical variables (Supplementary Note 1) comparing sequencing batches (batch 1, N=10; batch 2, N=26 subjects). **c,** Distribution of discrete metadata variables across sequencing batches; Fisher's exact tests (R stats::fisher.test, extended to r×c tables). **d,** 2D UMAP projection of snRNA-seq cells after quality control (N=102,710 cells), colored by selected metadata variables. **e,** Correlation of gene perturbation scores ($S = -\log_{10}(p) \times \text{sign}(\log_2(\text{fold-change}))$, unadjusted Limma-Voom p-values; N=24 controls, 12 LoF subjects), computed using all samples compared to excluding batch 2 (v2 chemistry). **a,b:** boxplots show median, IQR (box), and whiskers = 1.5×IQR.

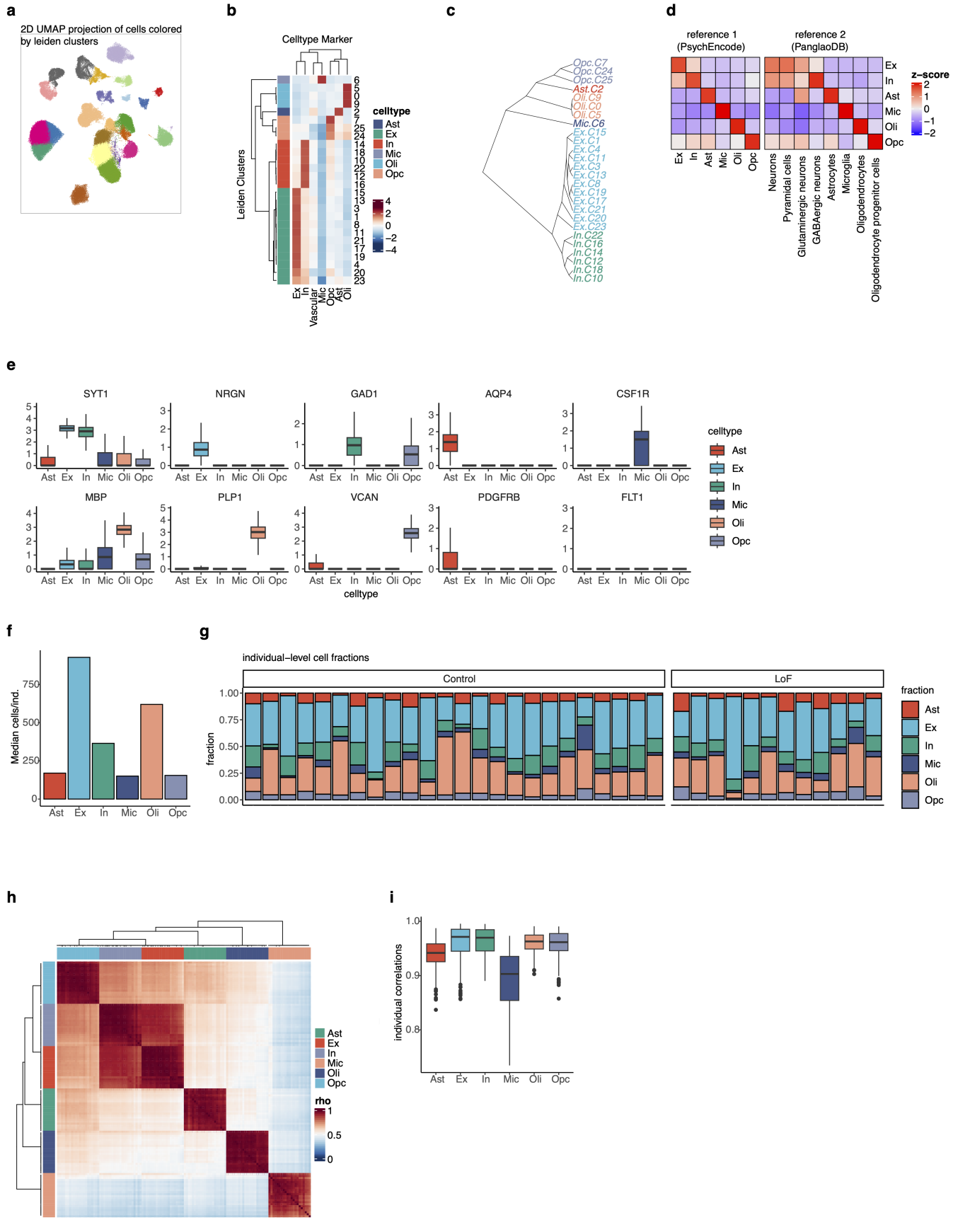
a
2D UMAP projection of cells colored by leiden clusters
b
Celltype Marker
Leiden Clusters
celltype
Ast
Ex
In
Mic
Oli
Opc
Ex
In
Vascular
Mic
Opc
Ast
Oli
c
Opc.C7
Opc.C24
Opc.C25
Ast.C2
Oli.C9
Oli.C0
Oli.C5
Mic.C6
Ex.C15
Ex.C1
Ex.C4
Ex.C11
Ex.C3
Ex.C13
Ex.C8
Ex.C19
Ex.C17
Ex.C21
Ex.C20
Ex.C23
In.C22
In.C16
In.C14
In.C12
In.C18
In.C10
d
reference 1 (PsychEncode)
reference 2 (PanglaoDB)
z–score
Neurons
Pyramidal cells
Glutaminergic neurons
GABAergic neurons
Astrocytes
Microglia
Oligodendrocytes
Oligodendrocyte progenitor cells
e
SYT1
NRGN
GAD1
AQP4
CSF1R
MBP
PLP1
VCAN
PDGFRB
FLT1
celltype
f
Median cells/ind.
g
individual–level cell fractions
Control
LoF
fraction
h
rho
i
individual correlations

Fig. S2. Overview of snRNA-sequencing cell type annotations. **a,** 2D UMAP projection of individual cells (N=102,710 cells, 36 subjects), colored by Leiden clusters. **b,** Average marker gene expression (mean log(fold-change) per cluster; colorbar) for cell types (x-axis). Fold-changes calculated for each cluster versus all others, using marker genes from Reference 1 (Supplementary Table 3). **c,** Cladogram of subcluster relationships based on pairwise distances of per-cluster gene expression profiles. **d,** Average marker gene expression profiles per major cell type (y-axis) across two marker gene references (Supplementary Table 3). **e,** Per-cell distribution of selected marker gene expression by cell type (log-counts; y-axis). **f,** Median number of cells per cell type per subject (N=36 subjects). **g,** Cell type fraction per subject (N=36 subjects). **h,** Heatmap showing correlations of individual-level gene expression profiles by cell type (N=36 subjects). **i,** Boxplots of individual-level gene expression correlations by cell type (N=36 subjects). **a-f:** N cells=Ex 42,014, In 14,806, Ast 7,158, Mic 5,441, Oli 28,078, Opc 5,213.

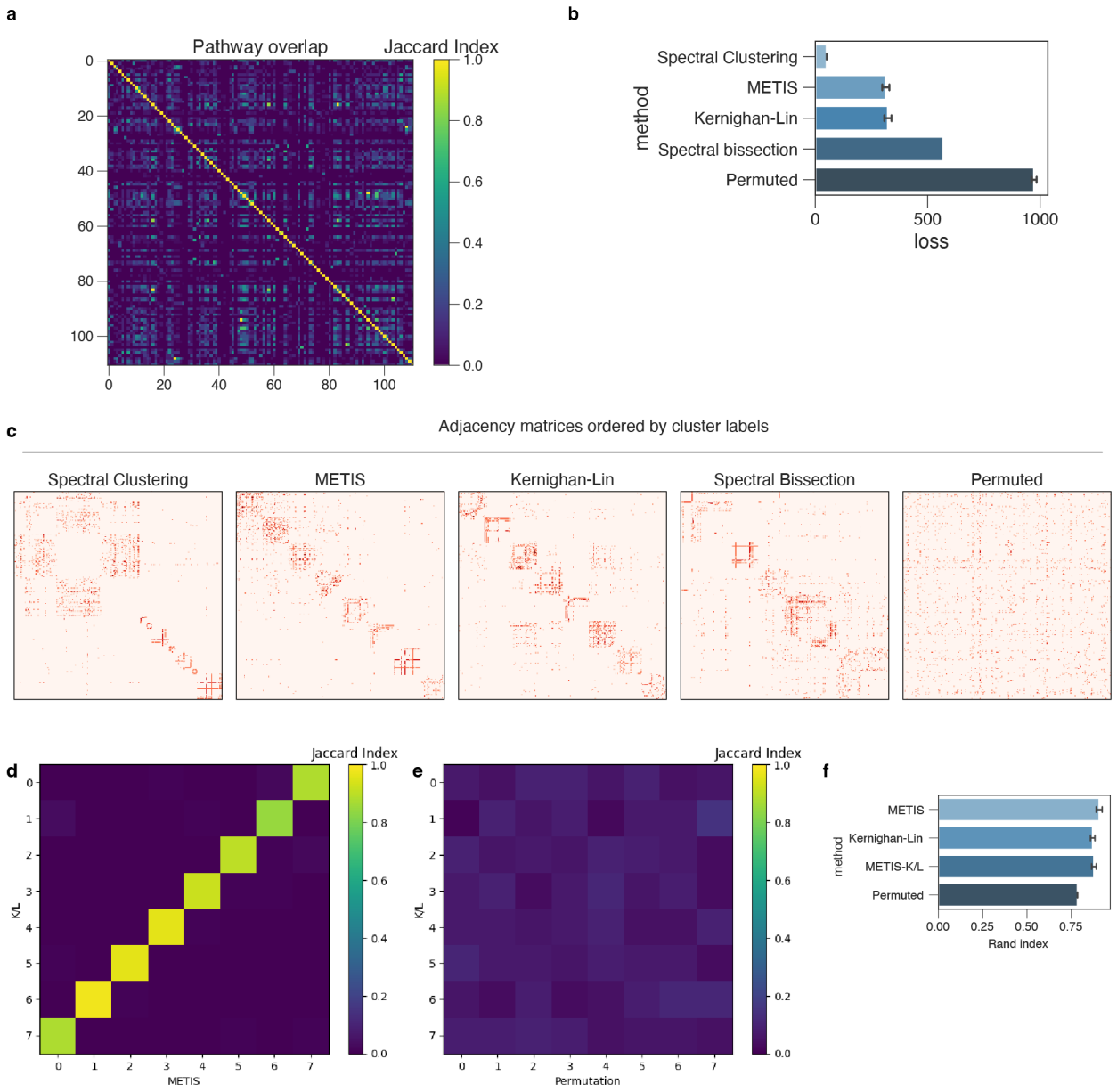

Fig. S3. Benchmarking partitioning and clustering algorithms for gene–pathway grouping.

a, Analysis of Jaccard overlap between pathways conducted on an $n \times p$ matrix, where the n pathways are a subset of the WikiPathways database that annotate more than four leading-edge (LE) genes as identified by fGSEA enrichment (unadjusted $p < 0.05$) comparing ABCA7 control versus LoF excitatory neurons (p total LE genes). **b,** Average loss (total cut size; Methods) from applying algorithms—spectral clustering (SC), METIS, Kernighan–Lin (K/L), spectral bisection (SB), and random permutation—to the graph G ($n + p = 379$ vertices; Methods). SC and random permutation were run over 1,000 initiations; METIS and K/L over 5×10^5 initiations. SB is deterministic and was run once. Error bars indicate standard deviations. **c,** Unweighted adjacency matrix of graph G, sorted by cluster labels assigned by each algorithm. Red indicates edges between vertices. Labels correspond to the best initiation (lowest loss) from 1,000 initiations (SC, random permutation) or

5×10^5 initiations (METIS, K/L). **d,** Pairwise labeling consistency between optimal K/L and optimal METIS initiations. Axes represent cluster labels from each method; color intensity reflects the fraction of shared vertices per cluster. **e,** Same as (d) but comparing optimal K/L and optimal random permutation initiations. **f,** Average Rand index (RI) across initiation pairs from (b). "METIS," "Kernighan–Lin," and "Permuted" on the Y-axis indicate mean RI (label consistency) within each algorithm. "METIS–K/L" indicates mean RI for pairwise comparisons between METIS and K/L. Error bars show standard deviations. $\text{RI} = \frac{\text{number of agreeing vertex pairs}}{\text{total vertex pairs}}$.

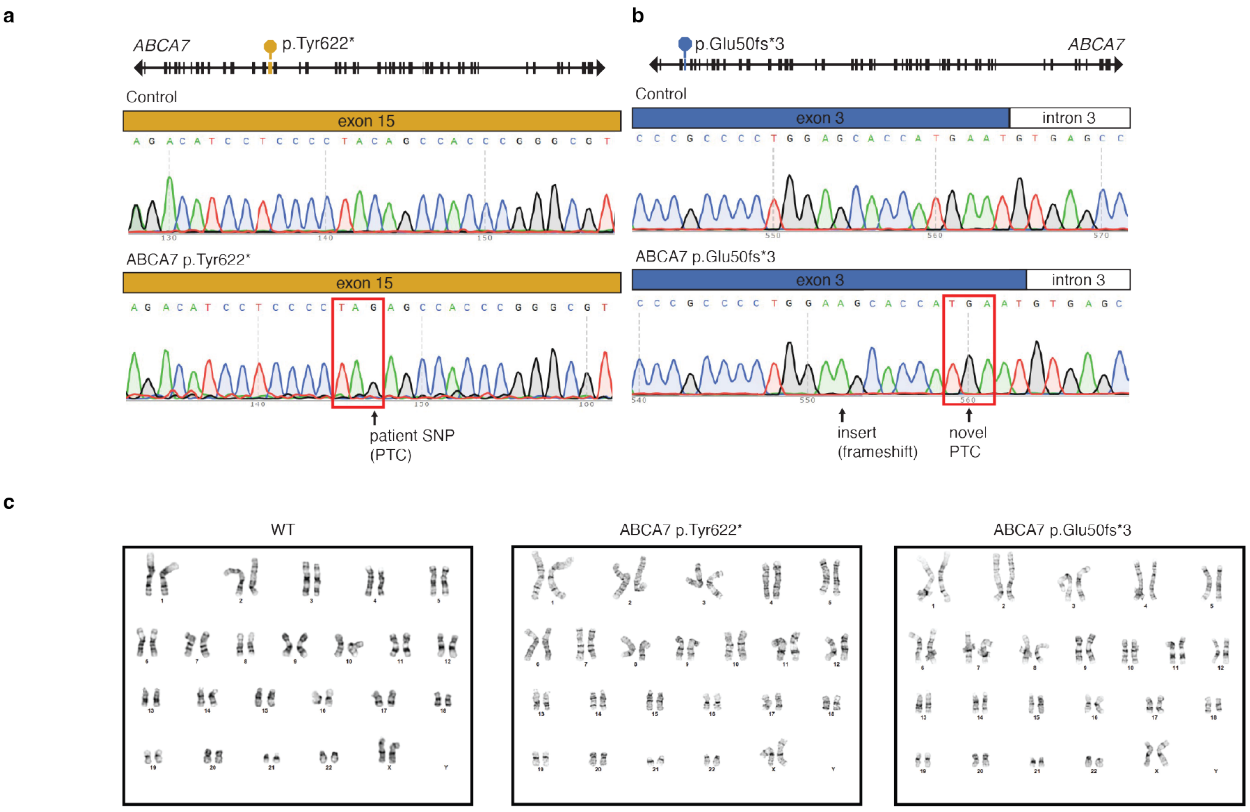

Fig. S4. Generation of iPSC-Derived Cells Harboring ABCA7 PTC Variants. **a,** Sanger sequencing chromatogram confirming patient single nucleotide polymorphism in ABCA7 exon 15 of the ABCA7 p.Tyr622* isogenic iPSC line (Adobe Illustrator). **b,** Sanger sequencing chromatogram confirming single nucleotide insertion in ABCA7 exon 3 of the ABCA7 p.Glu50fs*3 isogenic iPSC line (Adobe Illustrator). **c,** Normal karyotypes were observed for WT, ABCA7 p.Glu50fs*3, and ABCA7 p.Tyr622* isogenic iPSC lines. One experiment shown. Experiment performed regularly as part of quality control; see Methods.

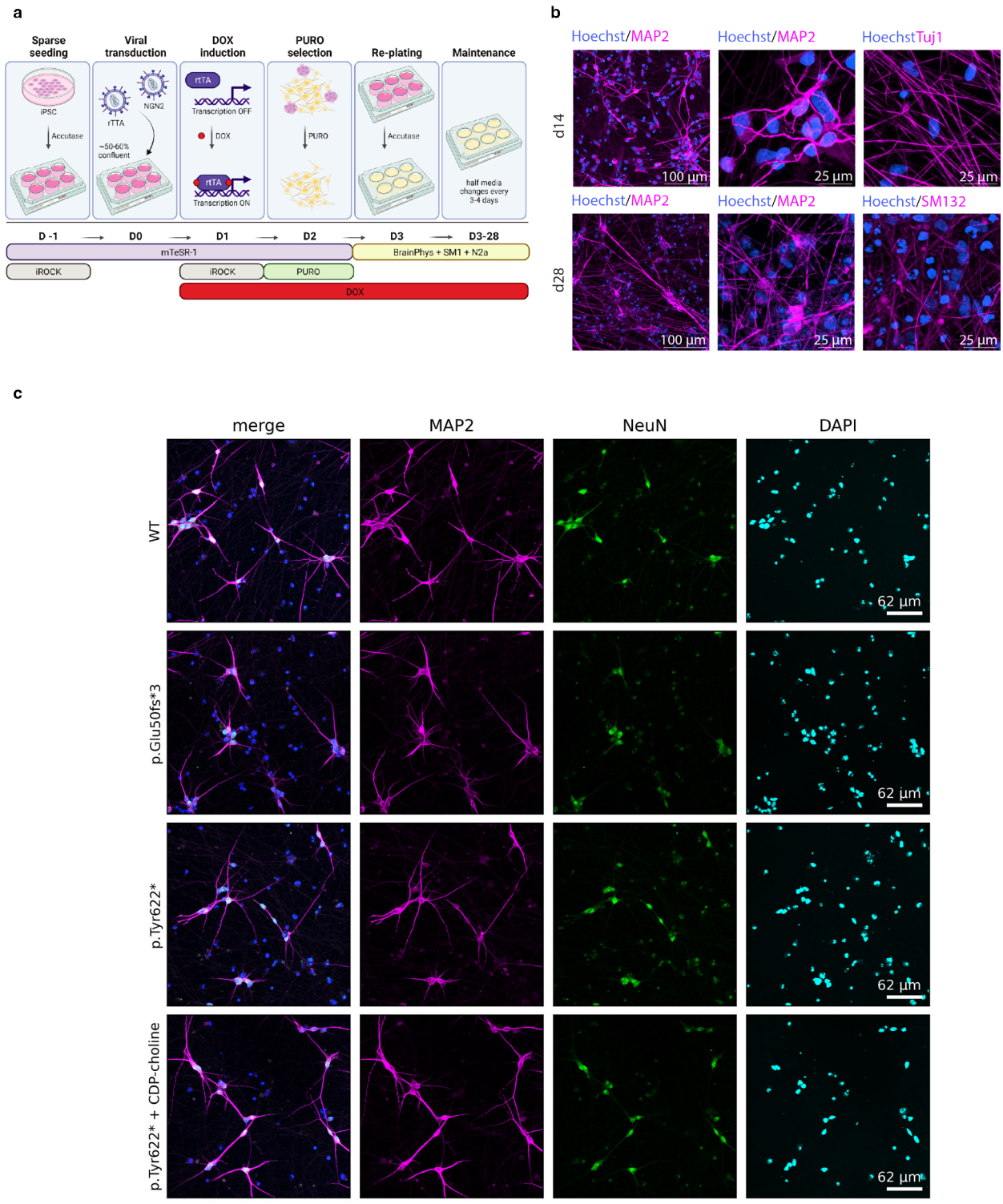

Fig. S5. Differentiating iPSC-Derived Neurons Harboring ABCA7 PTC Variants. **a,** iPSCs were plated at low density for NGN2 viral transduction. Expression of NGN2 was driven by doxycycline (DOX) induction with puromycin (PURO) selection, then cells were replated to match neuronal densities. Neurons were maintained for 4 weeks (DIV 28) before experimentation (BioRender

agreement # PA28FD1SCF). **b,** Neuronal marker expression in 2 and 4-week matured iNs. **c,** Neuronal marker expression in iNs matured for 4 weeks for indicated genotypes. CDP-choline treatment was applied for 2 weeks at 100 μM. **b,c:** Experiments performed once. Subset of these images shown in Fig. 3a.

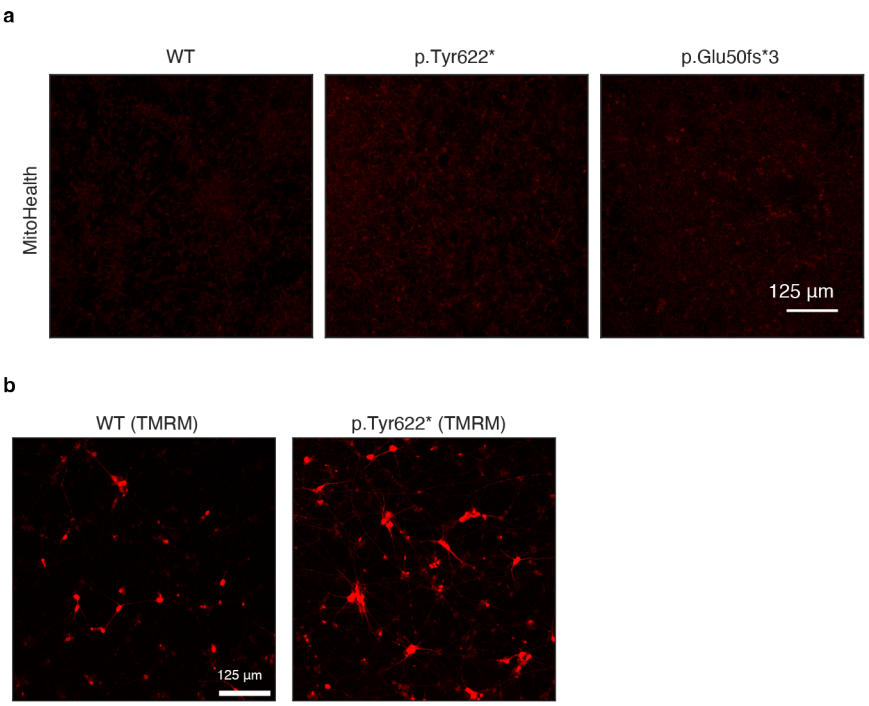

Fig. S6. Original unprocessed images of mitochondrial membrane potential without pseudocoloring. **a,** Maximum MitoHealth projections over z-axis. No other transformations applied. Same experiment as Fig. 3h. **b,** Mean TMRM projection over time. No other transformations applied. Same images and experiment as Fig. 3i.

Supplementary Tables

Supplementary Table 1. Overview of rare ABCA7 loss-of-function variants identified in the ROSMAP cohort. Columns include variant identifiers (rsID), coding sequence (HGVS.c) and protein (HGVS.p) notation (HGVS nomenclature), functional annotation, previously reported AD association, and number of carriers (N in cohort).

rsID	HGVS.c	HGVS.p	Annotation	AD association	N in cohort
rs113809142	c.4416+2T>G	NA	splice donor variant[75]	Steinberg et al (2015), Nature Genetics, Table 1[76]	1
rs200538373	c.5570+5G>C	NA	splice region variant[75,6]	Steinberg et al (2015), Nature Genetics, Table 1[76]	4
rs538591288	c.4208delT	p.Leu1403fs	frameshift variant[75]	Steinberg et al (2015), Nature Genetics, Table 1[76]	1
rs547447016	c.2126_2132delAGCAGGG	p.Glu709fs	frameshift variant[75]	Steinberg et al (2015), Nature Genetics, Table 1[76]	4
rs201060968	c.3641G>A	p.Trp1214*	stop gained	NA	1
19_1053362_G_A	c.3255G>A	p.Trp1085*	stop gained	NA	1

Supplementary Table 2. Annotation of ABCA7 loss-of-function variants identified in this study (all on chromosome 19). Columns include genomic position (POS), variant ID, reference (REF) and alternate (ALT) alleles, functional effect, coding sequence (HGVS_C) and protein-level (HGVS_P) annotations, and minor allele frequency (MAF).

POS	ID	REF	ALT	Effect	HGVS_C	HGVS_P	MAF
1047507	rs547447016	AGGAGCAG	A	frameshift variant	c.2126_2132delAGCAGGG	p.Glu709fs	0.0025
1053362	no known rsID	G	A	stop gained	c.3255G>A	p.Trp1085*	0.0004
1054255	rs201060968	G	A	stop gained	c.3641G>A	p.Trp1214*	0.0004

1055907	rs538591288	CT	C	frameshift variant & splice region variant	c.4208delT	p.Leu1403fs	0.0004
1056244	rs113809142	T	G	splice donor variant & intron variant	c.4416+2T>G	N/A	0.0008
1061892	rs200538373	G	C	splice region variant & intron variant	c.5570+5G>C	N/A	0.0021

Supplementary Table 3. External datasets used.

Description	Access	Reference
postmortem human PFC proteomic data	https://www.synapse.org/#!Synapse:syn21449368	[77]
ROSMAP WGS data	https://www.synapse.org/Synapse:syn11724057	N/A
Reference 1: Cell type specific marker genes for human brain	https://osf.io/pqr9m/	[78]
Reference 2: Cell type specific marker genes for human brain	https://osf.io/pqr9m/	[79]
Gene Ontology Biological Process 2023	https://maayanlab.cloud/Enrichr/#libraries	NA
NeuN+/- bulk RNA-sequencing from postmortem human brain	https://www.synapse.org/#!Synapse:syn33212353	[80]
WikiPathways 2019 Human	https://maayanlab.cloud/Enrichr/#libraries	NA
snRNAseq from postmortem human PFC from p.Ala1527Gly variant-carriers and controls	https://www.synapse.org/#!Synapse:syn52293417	[81]
Human MitoCarta3.0	https://www.broadinstitute.org/mitocarta/mitocarta30-inventory-mammalian-mitochondrial-proteins-and-pathways	NA
Human prefrontal cortex layer markers based transcriptomics on dissected layers	https://www.nature.com/articles/nn.4548#article-info	[82]

Human dorsolateral prefrontal cortex spatial transcriptomics markers	https://www.nature.com/articles/s41593-020-00787-0#article-info	[83]

Supplementary Table 11. Enriched mitochondrial pathways (MitoCarta) comparing WT vs. p.Tyr622* mRNA identified using the Python package `gseapy`. Columns include pathway terms, enrichment scores ($-\log_{10}$ P-value), raw and FDR-corrected p-values, and associated mitochondrial genes. Only results with $p < 0.05$ are shown.

Term	score	P-value	FDR	Genes
Apoptosis	1.900274	0.012581	0.415774	BID; CASP3; CYCS; BCL2L1; BIK
OXPHOS	1.894438	0.012752	0.415774	NDUFA4; TMEM126A; ATP5MG; SDHAF2; NDUFA1; COX6A1; COX14; CYCS; COA4; NDUFS4; ATP5PB; ATP5MC3; NDUFAF2; MT-ND2
Protein import and sorting	1.755279	0.017568	0.415774	TIMM8A; TIMM10; DNAJC19; SAMM50; TIMM23; TOMM22
OXPHOS subunits	1.552584	0.028017	0.477391	NDUFA4; ATP5MG; NDUFA1; COX6A1; CYCS; NDUFS4; ATP5PB; ATP5MC3; MT-ND2
Mitochondrial dynamics and surveillance	1.473414	0.033619	0.477391	BID; ATP5MG; SAMM50; CASP3; CYCS; BCL2L1; FUNDC1; BIK; FUNDC2
Amino acid metabolism	-1.374004	0.042267	0.263353	DLST; COMT; SLC25A44; MAOA; ABAT; SFXN3; GCAT; ALDH5A1; MCCC2; AADAT
Detoxification	-1.395286	0.040245	0.263353	EPHX2; DHRS2; CYB5B; CAT; TXNRD2; MAOA; CYB5R3
EF hand proteins	-1.441227	0.036205	0.263353	RHOT2; SLC25A23; SLC25A25
Lipid metabolism	-1.441792	0.036158	0.263353	EPHX2; SLC25A1; ACADVL; GPAT2; CPT1C; ACADL; IDI1; ACP6; CROT; CYB5R3; CYP27A1; ACAD10
Amidoxime reducing complex	-1.576863	0.026493	0.238440	CYB5R3; CYB5B
Vitamin metabolism	-1.639877	0.022915	0.232016	MMAB; DHRS4; PLPBP; PNPO; RFK; PC; SFXN3
Gluconeogenesis	-1.844185	0.014316	0.165654	PCK2; PC; SLC25A1
Catechol metabolism	-1.857772	0.013875	0.165654	COMT; MAOA
TCA-associated	-1.887037	0.012971	0.165654	ACLY; PCK2; PC; SLC25A1
ABC transporters	-2.026052	0.009418	0.165654	ABCB6; ABCD2; ABCB8
Xenobiotic metabolism	-2.103329	0.007883	0.165654	EPHX2; DHRS2; CYB5B; MAOA; CYB5R3
Vitamin B6 metabolism	-2.314663	0.004845	0.165654	PNPO; PLPBP

Metabolism	-4.519649	0.000030	0.002448	NMNAT3; DHRS4; CAT; GPAT2; DLAT; FECH; PNPO; SLC25A25; MCCC2; MMAB; COQ9; SLC25A1; PLPBP; ACLY; TXNRD2; ABAT; RFK; TK2; PC; IDI1; PCK2; EPHX2; DHRS2; ACADVL; IDH2; CPT1C; CROT; ALDH5A1; AADAT; ACAD10; TSTD1; CYB5B; DLST; SLC25A44; ABCB6; GATM; SLC25A23; MAOA; ACADL; SFXN3; ACP6; GCAT; COMT; CYP27A1; CYB5R3

Supplementary Table 14. Enriched mitochondrial pathways (MitoCarta) comparing p.Tyr622* + H_2O vs. p.Tyr622* + CDP-choline mRNA identified using the Python package `gseapy`. Columns include pathway terms, enrichment scores ($-\log_{10}$ P-value), raw and FDR-corrected p-values, and associated mitochondrial genes. Only results with $p < 0.05$ are shown.

Term	**score**	**P-value**	**FDR**	**Genes**
EF hand proteins	4.457699	0.000035	0.003451	SLC25A12; SLC25A23; SLC25A25; EFHD1; MICU2; SLC25A13; MICU3; SLC25A24
Small molecule transport	3.256577	0.000554	0.027418	ABCB10; SLC25A25; MPV17L; ABCD3; ABCD1; SLC25A12; SLC25A1; SLC25A13; MICU3; SFXN1; SLC25A29; SLC25A39; SLC25A43; MICU2; SFXN5; STARD7; SLC25A24; ABCD2; SLC25A15; SLC25A22; SLC25A23; VDAC1; MPV17
Calcium homeostasis	3.079591	0.000833	0.027474	SLC25A12; SLC25A23; SLC25A25; EFHD1; VDAC1; LETM1; SLC25A13; MICU2; MICU3; SLC25A24

Metabolism	2.846777	0.001423	0.033450	ABCB10; NT5DC2; ACSL6; ME3; CS; SLC25A12; PDSS2; HSD17B4; ACLY; TK2; ALDH3A2; IDI1; NADK2; ACADS; CPT2; STARD7; AADAT; ACAD10; AK3; NNT; SOD2; CHCHD7; SLC25A23; OGDH; NMNAT3; MT-CO1; GLS; GPAT2; SLC25A25; OAT; D2HGDH; SLC25A1; ABAT; RFK; SFXN1; ALDH1B1; OXCT1; TST; HIBCH; FHIT; FH; GLYCTK; LACTB; PNPO; SERAC1; ME2; GSR; AGPAT5; PCK2; SLC25A29; EPHX2; GLDC; SFXN5; PDK3; ALDH5A1; SPHK2; SLC25A24; TSTD1; MTFMT; ACP6; NT5M; ALDH9A1; GCAT; KMO; ECI1; CAT; DLAT; COQ2; PPM1K; PRXL2A; MCCC2; CISD3; SPTLC2; SLC25A13; SLC25A15; FASN; ALDH7A1; DLST; GATM; AK4; ACADSB
Signaling	2.772263	0.001689	0.033450	NLRX1; SLC25A12; PPTC7; SLC25A23; SLC25A25; EFHD1; VDAC1; LETM1; MACROD1; SLC25A13; MICU2; PDE2A; MICU3; SLC25A24; DELE1
TCA-associated	2.563737	0.002731	0.045055	SLC25A1; ACLY; ME2; SFXN5; ME3; D2HGDH; PCK2
Fusion	2.466941	0.003412	0.048261	OPA1; MIGA2; MFN2; MIGA1; MFN1
Carbohydrate metabolism	1.960909	0.010942	0.123756	OXCT1; CS; SLC25A12; SLC25A1; FH; DLAT; ACLY; ME2; GLYCTK; DLST; OGDH; SLC25A13; ME3; SFXN5; PDK3; D2HGDH; PCK2
Organelle contact sites	1.856642	0.013911	0.123756	FKBP8; SPIRE1; MIGA2; MFN2; MFN1; VDAC1
ABC transporters	1.852052	0.014059	0.123756	ABCB10; ABCD1; ABCD2; ABCD3
Phospholipid metabolism	1.850381	0.014113	0.123756	GPAT2; SERAC1; SPTLC2; LACTB; ACP6; STARD7; AGPAT5; SPHK2
Amino acid metabolism	1.823889	0.015001	0.123756	GLS; OAT; PPM1K; MCCC2; SLC25A12; ABAT; SLC25A13; SFXN1; SLC25A29; GLDC; ALDH5A1; AADAT; HIBCH; ALDH9A1; SLC25A15; ALDH7A1; DLST; GCAT; ACADSB; KMO
Nucleotide metabolism	1.357357	0.043918	0.334453	AK3; NT5DC2; SLC25A23; SLC25A25; GATM; AK4; TK2; NT5M; SLC25A24; FHIT

OXPHOS assembly factors	-1.423365	0.037725	0.363536	FOXRED1; TIMMDC1; COA3; COA6; COX7A2L; SDHAF3; FMC1; COX16; RAB5IF; NDUFAF6; SDHAF2; SURF1; TIMM21; BCS1L; COA7; NDUFAF1; COX14; LYRM2; TMEM70
Protein import and sorting	-1.445375	0.035861	0.363536	MTX2; TIMM8A; TIMM23; TIMM17B; TIMM10; UQCRC1; DNAJC19; PMPCA; TIMM8B; MTX1; TIMM21; TIMM22; TOMM5; GRPEL1
CIII subunits	-1.603039	0.024944	0.293782	UQCR10; CYC1; UQCRH; UQCRC1; UQCRFS1
mtRNA granules	-1.605563	0.024799	0.293782	MRPL47; ERAL1; MTPAP; ALKBH1; PTCD2; MRPS7; TFB1M; TRUB2; RMND1; TRMT10C
CII subunits	-1.645356	0.022628	0.293782	SDHD; SDHC; SDHB
Complex II	-2.114075	0.007690	0.135856	SDHAF2; SDHAF3; SDHC; SDHB; SDHD
OXPHOS subunits	-2.580372	0.002628	0.055714	UQCR10; ATP5MG; SDHB; ATP5PB; UQCRH; NDUFA10; COX5B; COX7A2L; NDUFB3; NDUFA4; CYC1; SDHD; MT-ND4L; UQCRFS1; ATP5IF1; NDUFA1; NDUFV1; COX6A1; NDUFB8; ATP5F1A; SDHC; NDUFB6; NDUFA6; NDUFS4; COX7A2; UQCRC1; NDUFS2; ATP5F1C
Mitochondrial central dogma	-2.864986	0.001365	0.036163	MRPL4; MRPL18; COA3; MTRES1; MRPL46; MTIF3; MRPS23; MRPL37; MRPL45; MRPL36; TRUB2; MRPS10; MRPL24; PTCD2; MRPL40; MRPS18C; UNG; TFB1M; METTL5; MRPS12; MRPL14; GATC; MRPL34; MRPL32; MRPL16; TSFM; MTPAP; MRPL47; APEX1; MRPS21; ALKBH1; TEFM; MRPL55; MRPL39; MRPS7; MRPS26; MRPL22; TIMM21; MRPL15; MTERF2; NGRN; MRPS18A; TRMT10C; MTERF1; ERAL1; MRM3; COX14; MRPS31; MRPL13; PTCD3; MRPS14; DAP3; MTERF3; MRPL27; MRPS28; RARS2; MRPS18B; RMND1; MRPS15

OXPHOS	-3.420637	0.000380	0.013414	UQCR10; FOXRED1; TIMMDC1; ATP5MG; COA3; SDHB; ATP5PB; UQCRH; NDUFA10; COX5B; COA6; COX7A2L; NDUFB3; NDUFA4; CYC1; SDHAF3; FMC1; SDHD; MT-ND4L; UQCRFS1; ATP5IF1; RAB5IF; COX16; NDUFAF6; SDHAF2; SURF1; NDUFV1; NDUFA1; COX6A1; TIMM21; NDUFB8; BCS1L; COA7; NDUFA12; NDUFAF1; ATP5F1A; COX14; SDHC; NDUFA6; NDUFB6; LYRM2; NDUFS4; COX7A2; UQCRC1; TMEM70; NDUFS2; ATP5F1C
Translation	-4.653989	0.000022	0.001176	MRPL4; MRPL18; COA3; MTRES1; MRPL46; MTIF3; MRPS23; MRPL37; MRPL45; MRPL36; MRPS10; MRPL24; MRPL40; MRPS18C; TFB1M; MRPS12; MRPL14; GATC; MRPL34; MRPL32; MRPL16; TSFM; MRPL47; MRPS21; MRPL55; MRPL39; MRPS7; MRPS26; MRPL22; TIMM21; MRPL15; NGRN; MRPS18A; ERAL1; MRM3; COX14; MRPS31; MRPL13; PTCD3; DAP3; MRPS14; MTERF3; MRPL27; MRPS18B; RARS2; MRPS28; RMND1; MRPS15
Mitochondrial ribosome	-6.408523	0.000000	0.000041	MRPL4; MRPL18; MRPL46; MRPS23; MRPL37; MRPL45; MRPL36; MRPS10; MRPL24; MRPL40; MRPS18C; MRPS12; MRPL14; MRPL34; MRPL32; MRPL16; MRPL47; MRPS21; MRPL55; MRPL39; MRPS7; MRPS26; MRPL22; MRPL15; MRPS18A; MRPS31; MRPL13; PTCD3; DAP3; MRPS14; MRPL27; MRPS18B; MRPS28; MRPS15

Supplementary Table 15. Experimentally determined 3D ABCA7 structures used in molecular dynamics simulations. Columns include system description (System), Protein Data Bank identifier (PDB ID), and conformational state (State).

System	PDB ID	State
CLOSE-G1527	8EOP	HOLO
CLOSE-A1527	8EOP	HOLO
OPEN-G1527	8EE6	APO

OPEN-A1527	8EE6	APO

Supplementary Table 16. Primers used for PCR and Sanger sequencing (SS). Columns indicate primer names (Primer) and their nucleotide sequences (Sequence).

Primer	Sequence
rs547447016_FOR	5'-ACGCTGGCCTGGATCTACTC-3'
rs547447016_REV	5'-TGCATGCGTGTGCCAAGAAG-3'
chr19.1053362G>A_rs201060968_FOR	5'-CTGAAGCACCCCTTTGTCCAC-3'
chr19.1053362G>A_rs201060968_REV	5'-GAAAGCGCTTGAGAAGCAGGG-3'
chr19.1053362G>A_REV_SS	5'-GCTGCTCATAAACACGCTATTCATCCTTC-3'
rs201060968_FOR_SS	5'-CATTGCTGGCCTAGACGTAA-3'
ABCA7_p.Glu50fs*3_FOR	5'-GTGACGAAAGCGTTAAGCCC-3'
ABCA7_p.Glu50fs*3_REV	5'-GCAGTGGCTTGTTTGGGAAG-3'
ABCA7_p.Tyr622*_FOR	5'-CTGGTTCTGGTGCTCAAG-3'
ABCA7_p.Tyr622*_REV	5'-CCTACGGCAGACGTCTTCAG-3'

Supplementary Table 17. Antibodies used.

Antibody name	Company	Catalog No.
NeuN	Synaptic Systems	266004
Tuj1	BioLegend	MMS-435P
SM312	Biolegend	837904
MAP2	Biolegend	822501

SI References

71. Bennett, D. A. *et al.* en. *J. Alzheimers. Dis.* **64,** S161–S189 (2018).
72. Elsner, U. *Graph Partitioning: A Survey* 1997.
73. Karypis, G. & Kumar, V. *METIS: A Software Package for Partitioning Unstructured Graphs, Partitioning Meshes, and Computing Fill-Reducing Orderings of Sparse Matrices* Technical Report TR-97-065. Accessed: 2025-03-28 (University of Minnesota, Department of Computer Science, 1997).
74. Kernighan, B. W. & Lin, S. *Bell Syst. Tech. J.* **49,** 291–307 (Feb. 1970).
75. Allen, M. *et al.* en. *Neurol. Genet.* **3,** e126 (Feb. 2017).
76. Steinberg, S. *et al.* en. *Nat. Genet.* **47,** 445–447 (May 2015).
77. Johnson, E. C. B. *et al.* en. *Nat. Med.* **26,** 769–780 (May 2020).
78. Wang, D. *et al.* en. *Science* **362,** eaat8464 (Dec. 2018).
79. Franzén, O., Gan, L.-M. & Björkegren, J. L. M. en. *Database (Oxford)* **2019** (Jan. 2019).
80. Welch, G. M. *et al.* en. *Sci Adv* **8,** eabo4662 (Sept. 2022).
81. Mathys, H. *et al.* en. *Cell* **186,** 4365–4385.e27 (Sept. 2023).
82. He, Z. *et al.* en. *Nat. Neurosci.* **20,** 886–895 (June 2017).
83. Maynard, K. R. *et al.* en. *Nat. Neurosci.* **24,** 425–436 (Mar. 2021).